Automatic Estimation of Purkinje-Myocardial Junction hot-spots from Noisy Endocardial Samples: A simulation study

Fernando Barber* | Ignacio García-Fernández | Miguel Lozano | Rafael Sebastian

[1]Computational Multiscale Simulation Lab (CoMMLab), Departament d'Informàtica, Universitat de València, 46100 Burjasot, Spain

Correspondence
*Fernando Barber, Departament d'Informàtica, ETSE, Universitat de València, 46100 Burjasot (Valencia), Spain.
Email: fernando.barber@uv.es

Abstract

The reconstruction of the ventricular cardiac conduction system (CCS) from patient-specific data is a challenging problem. High-resolution imaging techniques have allowed only the segmentation of proximal sections of the CCS from images acquired ex-vivo. In this paper we present an algorithm to estimate the location of a set of Purkinje-myocardial junctions from electro-anatomical maps, as those acquired during radio-frequency ablation procedures. The method requires a mesh representing the myocardium with local activation time measurements on a subset of nodes. We calculate the backwards propagation of the electrical signal from the measurement points to all the points in the mesh to define a set of candidate PMJs, that is iteratively refined. The algorithm has been tested on several Purkinje network configurations, with simulated activation maps, subject to different error amplitudes. The results show that the method is able to build a set of Purkinje-myocardial junctions that explain the observed activation map for different synthetic CCS configurations. In the tests, the average error in the predicted activation time is below the amplitude of the error applied to the data.

KEYWORDS:
Cardiac Conduction System; Purkinje Tree; Electro-Anatomical Map; Patient-Specific Modelling; Cardiac Electrophysiology

1 | INTRODUCTION

Computational modelling of the heart has made important contributions to the understanding of cardiac electrophysiology, such as unveiling underlying mechanisms of arrhythmia (1, 2, 3) or proposing novel tools for patient risk stratification (4). The multiscale biophysical models of the heart allow to model cardiac electrophysiology from cell to body scale. When those models are combined with three-dimensional representations of the heart, it is possible to simulate heart function with a great level of detail, and to perform experiments that could be impossible in a real clinical setting (2, 5). However, the utility of the models relies on its accuracy and fidelity to reproduce experimental or clinical results, and therefore they have to be tailored to fit available data.

There are two fundamental sources of data to adjust the models, the so-called patient-specific data, and population-based data. Patient-specific data are acquired from each individual, and are limited to the clinical invivo techniques available in each medical centre. On the other hand population-based data comprise all the data collected from invivo and exvivo experiments in several species for years. These data are very useful since most of the information required for the models cannot be retrieved easily, however, its use is opposed to the patient-specific philosophy. For instance, the arrangement of cardiomyocytes in the atria and

ventricles follows a specific configuration that has been studied both in animal and human hearts (6, 7), and has permitted the definition of mathematical models that describe it (8). In order to obtain the patient-specific fibre orientation of the ventricular tissue, non-trivial techniques such as diffusion tensor MRI have to be employed (9). However, due to the long acquisition times required and the fact that the heart is beating only a few heart planes can be imaged invivo, and the rest have to be interpolated, which hampers the original goal.

Another important component of heart models for cardiac electrophysiology is the cardiac conduction system (CCS) that has been traditionally neglected or modeled from population-based data published in the literature (10, 11). The CCS comprises the sino-atrial node, the heart's pacemaker, located in the atria; the atrio-ventricular node, that communicates the electrical impulse from the atria to the ventricles; the His bundle and the right and left bundle branches that diverge the impulse to both ventricles through the septal wall; and finally the Purkinje network (PKN), that functions as a highway that spreads at fast speed the electrical impulse across the ventricular muscle, and connects to the working myocardial tissue at discrete locations called Purkinje-myocardial junctions (PMJs) (12). Therefore, the activation of the ventricular tissue is dictated by the Purkinje system morphology and the relative time of PMJ activation. The PKN has been described macroscopically from photographs, microCT imaging (13), and microscopically from histological samples, in different species such as rabbit (14) and pig (15). Even though there have been comprehensive studies of the PKN (11), there are only few studies that aim at quantifying the location and density of PMJs, and they are usually performed in animals (15). The PKN is necessary in a computer model of the heart, to simulate not only the normal activation, but also a number of pathologies such as left bundle branch block, or sustained ventricular tachycardia macro-reentries (16, 17, 18, 19) in which the PKN is retrogradely activated and used to transport the electrical impulse (20).

Despite the interaction of the PKN with disease (16, 21), therapies (20, 22) and drugs (5), most modellers have opted for paying little attention to it, and instead have indirectly considered its function by altering the model's endocardial properties. Others have considered the PKN as an independent endocardial structure connected to the ventricular model, but have overlooked the complex morphology of the network (20), or have based it on macroscopic animal studies (10). More recent studies have started to use patient-specific data obtained from electro-anatomical maps (EAMs) of the ventricles (23, 24). The local activation time maps obtained from EAMs can be used to estimate the location of PMJs, and therefore, to somewhat personalize the PKN in a ventricular model (25, 26, 27). In addition, in some studies such as (24), the PKN was further personalized not only to match the normal activation from PKN to the myocardium, but also for cases in which the PKN is activated retrogradely from an abnormal ectopic focus out of the atrio-ventricular node.

In this work, we present a novel method to estimate the location of PMJs from EAMs directly on a 3-dimensional representation of the ventricles. The algorithm can track back the activation sources on the endocardium and approximate their location and corresponding activation times. The estimation method explicitly considers the uncertainty associated to the samples used to estimate the PMJs. These errors may arise from the positioning error (tip of the recording catheter) of the acquisition system or the error in annotating the local activation times (LATs) from the bipolar and unipolar signals.

2 | MATERIAL AND METHODS

We will consider synthetic Purkinje scenarios on 2-dimensional and 3-dimensional domains, that represent the ventricular-endocardium surface as a Riemannian manifold. Note that since the PKN is comprised with the endocardial layer, we do not need to consider the myocardial volume in our analysis. In our method, the inputs are the local tissue activation times at a set of scattered measurement points. The activation time and location of measurement will be subject to some error with known standard deviation σ. From this information, our goal will be to estimate a set of electrical source points on the mesh (i.e. PMJs) that explains the observed activation times.

2.1 | PMJ characterization

The ventricular endocardium is represented by a surface Ω embedded in $\mathbb{R}^3$. We will consider the geodesic distance in Ω with the metric inherited from $\mathbb{R}^3$. We assume that the activation of the ventricular CCS triggers at certain (unknown) source points, i.e. PMJs, the tissue depolarization that spreads through the endocardial surface at a speed v (we neglect the transmural electrical propagation). At a given location $\mathbf{p} \in \Omega$, we define its activation time as

$$t(\mathbf{p}) = \min_{\mathbf{s} \in S} \left(\tau(\mathbf{s}) + \frac{d(\mathbf{p}, \mathbf{s})}{v} \right), \tag{1}$$

where S is the set of source points, $\tau(\mathbf{s})$ the activation time of source $\mathbf{s} \in S$ and $d : \Omega \times \Omega \to \mathbb{R}$ is the geodesic distance on Ω. Note that the activation time for each source is specific. We will say that $\mathbf{s}$ *has activated* a location $\mathbf{p} \in \Omega$ if the minimum in (1) is achieved for $\mathbf{s}$.

We consider a finite set $\mathcal{P} \subset \Omega$ representing N measurement points $\mathbf{p}_i, \ i = 1, \dots, N$. For every measurement point, $\mathbf{p}_i \in \mathcal{P}$, its measured Local Activation Time (LAT) is given by $t_i = t(\mathbf{p}_i) + Z$, where Z is a Gaussian random variable $Z \sim N(0, \sigma^2)$. For a source point, $\mathbf{s}$ we define the set $A(\mathbf{s}) = \{\mathbf{p}_i : \mathbf{p}_i \text{ has been activated by } \mathbf{s}\}$, and the set of indexes $I_A(\mathbf{s}) = \{k : \mathbf{p}_k \in A(\mathbf{s})\}$. Indeed, these sets can be defined for any point $\mathbf{x} \in \Omega$, even if $\mathbf{x} \notin S$, but $A(\mathbf{x}) = I_A(\mathbf{x}) = \emptyset$ if $\mathbf{x}$ has not activated any measurement point.

Let us now consider an arbitrary point $\mathbf{x} \in \Omega$. If $\mathbf{x}$ is actually a source point, and $\mathbf{p}_i \in A(\mathbf{x})$ has activation time t_i, then, by propagating the signal backwards from $\mathbf{p}_i$ to $\mathbf{x}$, the activation time for $\mathbf{x}$ can be estimated as $a_i(\mathbf{x}) = t_i - d(\mathbf{p}_i, \mathbf{x})/v$. This estimation will have a Gaussian error due to Z. If we propagate the signal from every point in $\mathcal{P}$ onto $\mathbf{x}$, we will have the set $\mathcal{T}(\mathbf{x}) = \{a_i(\mathbf{x}) : i \in 1, \dots, N\}$. This set can be partitioned into the two disjoint subsets $\mathcal{T}(\mathbf{x}) = \mathcal{T}_A(\mathbf{x}) \cup \mathcal{T}_{NA}(\mathbf{x})$, where

$$\mathcal{T}_A(\mathbf{x}) = \{a_i(\mathbf{x}) : i \in I_A(\mathbf{x})\}; \qquad \mathcal{T}_{NA}(\mathbf{x}) = \{a_i(\mathbf{x}) : i \notin I_A(\mathbf{x})\}. \tag{2}$$

For all the time estimations $a_i \in \mathcal{T}_A(\mathbf{x})$, coming from points activated by $\mathbf{x}$, we have that

$$a_i(\mathbf{x}) = t_i - \frac{d(\mathbf{p}_i, \mathbf{x})}{v} = \tau(\mathbf{x}) + \frac{d(\mathbf{p}_i, \mathbf{x})}{v} + Z - \frac{d(\mathbf{p}_i, \mathbf{x})}{v} = \tau(\mathbf{x}) + Z, \tag{3}$$

where $\tau(\mathbf{x})$ is the actual (unknown) activation time of $\mathbf{x}$. Thus, all these values are samples of the same Gaussian random variable $a_i \sim N(\tau(\mathbf{x}), \sigma^2)$.

On the contrary, for any value $a_i \in \mathcal{T}_{NA}$, the associated value of t_i depends on the source $\mathbf{s}$ that activated $\mathbf{p}_i$ and on the distance from $\mathbf{p}_i$ to $\mathbf{s}$

$$a_i(\mathbf{x}) = t_i - \frac{d(\mathbf{p}_i, \mathbf{x})}{v} = \tau(\mathbf{s}) + \frac{d(\mathbf{p}_i, \mathbf{s})}{v} + Z - \frac{d(\mathbf{p}_i, \mathbf{x})}{v} \tag{4}$$

and, as a consequence, the values of these a_i are random variables with mean values μ_i that will not be, in general, equal. The values $a_i \in \mathcal{T}_{NA}$ will have an additional property; since point $\mathbf{p}_i \notin A(\mathbf{x})$, it has not been activated by $\mathbf{x}$, and we have by definition of t_i,

$$t_i \leq \tau(\mathbf{x}) + \frac{d(\mathbf{p}_i, \mathbf{x})}{v}, \tag{5}$$

and, then, for the value of a_i we have that

$$a_i(\mathbf{x}) = t_i - \frac{d(\mathbf{p}_i, \mathbf{x})}{v} \leq \tau(\mathbf{x}) + \frac{d(\mathbf{p}_i, \mathbf{x})}{v} + Z - \frac{d(\mathbf{p}_i, \mathbf{x})}{v} = \tau(\mathbf{x}) + Z \tag{6}$$

and all $a_i \in \mathcal{T}_{NA}(\mathbf{x})$ are Gaussian random variables with mean $\mu_i \leq \tau(\mathbf{x})$.

As stated earlier, this development is valid whether $\mathbf{x}$ is a source point or not. But in the former case, the set $\mathcal{T}_A(\mathbf{x})$ is empty and all the values in $\mathcal{T}(\mathbf{x})$ are variables with mean values given by Equation (4). To define our method, we propose a characterization of source points based on this property; our goal is to find those points $\mathbf{s} \in \Omega$ for which the set $\mathcal{T}_A(\mathbf{s})$ is not empty.

In Figure 1 we show the distribution of values of $\mathcal{T}(\mathbf{x})$ in different simulated scenarios. The leftmost histogram shows the distribution of $\mathcal{T}(\mathbf{s})$ at the source point $\mathbf{s}$, for a scenario with a single source point, showing a frequency distribution consistent with a normal distribution. In the middle figure, we show the frequency distribution of $\mathcal{T}(\mathbf{s})$ at a source point $\mathbf{s}$, in a scenario with two source points, showing a tail on the left side of the histogram. This tail corresponds to the values in $\mathcal{T}_{NA}(\mathbf{s})$, which in this case are measurement points activated by the second source. The rightmost histogram shows again the distribution of the whole set $\mathcal{T}$ for a non-source point, $\mathbf{x}$, in the scenario with two source points. Since $\mathbf{x}$ has not activated any measurement point $\mathcal{T}_A(\mathbf{x}) = \emptyset$ and the distribution shown actually corresponds to the values of $\mathcal{T}_{NA}(\mathbf{x})$.

This characterization identifies those source points that have activated a minimum number of measurement points so that it is possible to observe them as a peak in the histogram, see Figure 1 central panel. Indeed, we consider as non-source any point where the set $\mathcal{T}_A$ is not higher than a given threshold. This property makes it possible to identify sources that explain the observation $\mathcal{P}$. But the total number of sources that can be identified depends on the size and distribution of this observation. This issue will be discussed in the results section.

2.2 | Algorithm description

In our numerical approach, we have a discretization of the domain Ω formed by a triangular mesh, M. The set of measurement points $\mathcal{P}$ is formed by some of the vertices of this triangular mesh. Note that in a real clinical setting, the mesh is built from
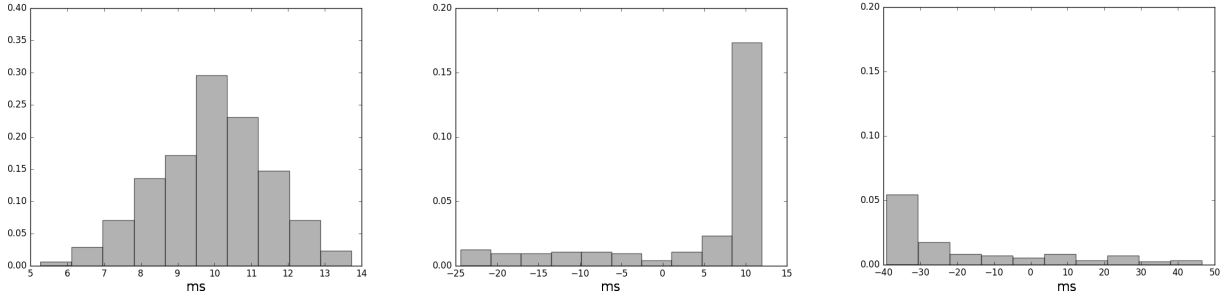
FIGURE 1 Distribution of the values of a_i for a simulated scenario. Left histogram shows all the values of $a_i \in \mathcal{T}(\mathbf{s})$ at a source point $\mathbf{s}$ in a scenario with a single source point. Central histogram shows all the values $a_i \in \mathcal{T}(\mathbf{s})$ at a source point $\mathbf{s}$ in a scenario with two source points. Right histogram shows the values $a_i \in \mathcal{T}(\mathbf{x}')$ at a point $\mathbf{x}'$ that is not a source point. Noise in all scenarios was included using a Gaussian with a standard deviation of 1.5.
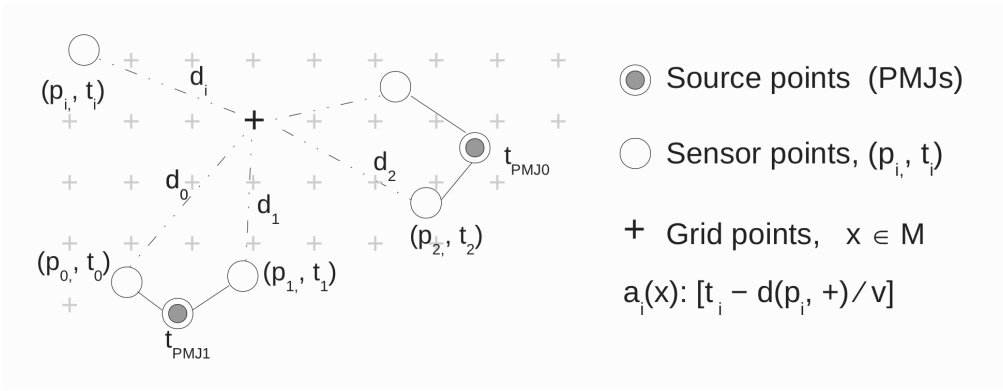
FIGURE 2 Simplified grid scenario. Measurement points are defined by the position p_i and their LAT t_i. Distance between measurements points and any point of the grid, d_i, is obtained by the Fast Marching algorithm.

the measurement points $\mathcal{P}$ and therefore they are always nodes of the final mesh. Every measurement point $\mathbf{p}_i \in \mathcal{P}$ has a local activation time, t_i (see Figure 2). Our method will result in a set $\mathcal{S}$ of estimated source points that will also be vertices of the mesh.

We propose a method with two main steps, described in Algorithm 1 and Algorithm 2. In the first step (Algorithm 1), we look for a set of PMJ checking if a mesh point $\mathbf{x}$ can be a source point according to the characterization described in Section 2.1 and the measured data. In a second step, once a set of estimated sources has been built, we will reduce the number of estimated PMJs by removing points that are in the neighbourhood of other estimated PMJ and that have a small influence on the activation map prediction. This step is described in Algorithm 2.

At the beginning of the first step, given the set of all measurement points $\mathbf{p}_i \in \mathcal{P}$, we compute the geodesic distance between every point in the triangle mesh M and every point in $\mathcal{P}$. To do so, we simulate the propagation of a signal from every point in $\mathbf{p}_i \in \mathcal{P}$ by solving the isotropic Eikonal equation (28) as in (26) by a fast marching algorithm (29). This geodesic distance computation is performed only once, before we start the estimation of the set $\mathcal{S}$. Note that since we are using the isotropic Eikonal equation, distances and activation times on the mesh nodes are proportional. Figure 2 shows a simplified scenario, where the discretization is represented by a regular grid on a flat domain, and the distances d_i are obtained for every pair of measurement point and grid point.

Using the t_i of all the measurement points $\mathbf{p}_i \in \mathcal{P}$ and the computed distances, we estimate the backwards activation time for each point $\mathbf{x}$ in the mesh, $a_i(\mathbf{x})$ (lines 2 and 3 in Algorithm 1). As a result, we have the set $\mathcal{T}(\mathbf{x})$ for every point in the discretized domain. Next, the method will examine this set for every point $\mathbf{x} \in M$, to decide whether it can be considered a source point,

---

Algorithm 1 Estimation of candidate electrical sources from measurement points

---

1: **for all** $\mathbf{x} \in M$ **do**
2:     $\mathcal{T} \leftarrow [a_i(\mathbf{x}) : a_i(\mathbf{x}) = t_i - d(p_i, x)/v \quad \forall (p_i, t_i) \in Measurement Points]$
3:     $\mathcal{T} \leftarrow sort(\mathcal{T}, decreasing)$
4:     $\mathcal{T}_{ok} \leftarrow \mathcal{T}[1:n] : Test(\mathcal{T}[1:n])$
5:     **if** $(n \geq 3)$ **then**   ▷ Focus candidate if there are at least 3 compatible measurement points
6:         Add $(\mathbf{x}, \mathcal{T}_{ok})$ to $listCSP$
7:     **end if**
8: **end for**
9: **Output** $\leftarrow listCSP$

---

i.e. if we have a nonempty set $\mathcal{T}_A(\mathbf{x})$ for each point $\mathbf{x} \in M$ (line 4 of the pseudocode). We know, from equation (6), that the variables in $\mathcal{T}_A(\mathbf{x})$ have a common mean that is higher than any mean values of the variables in $\mathcal{T}_{NA}(\mathbf{x})$. Thus, we will take the n largest values of $\mathcal{T}(\mathbf{x})$. Let $\mathcal{T}_n$ be the subset of $\mathcal{T}(\mathbf{x})$ with the n largest values. If the values in $\mathcal{T}_n$ have been generated by a common Gaussian distribution, with standard deviation σ and unknown mean value $\tau(\mathbf{x})$, we can assume that $\mathcal{T}_n \subseteq \mathcal{T}_A$.

This test will be performed for increasing values of n, until we reach the one for which the times in $\mathcal{T}_n$ set are not consistent with a Gaussian distribution. If the test indicates that $\mathcal{T}_n \subset \mathcal{T}_A(\mathbf{x})$ for at least, $n = 1, 2, 3$, then we will consider that $\mathcal{T}_A(\mathbf{x}) \neq \emptyset$ and as a consequence, $\mathbf{x} \in (S)$ (lines 5-7 of Algorithm1). The reason why three positive tests are requested is that at least three measurement points are required to exactly compute a source in absence of noise in the data (27). This value could be increased, to require a higher value of n before a point is considered to be a source, reducing the number of estimated points.

The main decision in Algorithm 1 relies on the test to decide whether a set of values $\mathcal{T}_n$ is a sample of a Gaussian distribution (line 4). The natural approach to perform this test would be a hypothesis contrast, or a normality test. However, in our problem, the size of the sample will be, in general, small $(n < 10)$ since the total number of measurement points will be of hundreds or, in the best cases, of a few thousands. Depending on the number of PMJs in the scenario, the value of $|\mathcal{T}_A|$ will be rather small for most of the source points. Taking into account these considerations, we find that most tests will not meet the requirements to perform a significant hypothesis contrast. In turn, we will focus on the fact that we know the standard deviation, σ, of the values in $|\mathcal{T}_A|$ and we set the following criterion to test if $\mathcal{T}_n \subset \mathcal{T}_A$. Given a point $\mathbf{x} \subset M$ and an $n \geq 3$, we compute the mean of the $a_i(\mathbf{x})$, denoted as $\bar{t}_n$, and we consider that the point $\mathbf{x}$ is a candidate source point, $\mathbf{x} \in S$, if

$$\max_{a_i \in \mathcal{T}_n}(|a_i - \bar{t}_n|) \leq \alpha\sigma,$$

with α a parameter to determine the sensitivity of the decision and σ the standard deviation of the measurements, defined in Section 2.1. If the point $\mathbf{x}$ meets this criterion, it is stored in the list $listCSP$ and it is assigned the activation time $t(\mathbf{x}) = \bar{t}_n$. Along with each possible source point, we store the largest value of n for which we obtain a positive result and the set of points $\mathbf{p}_i$ associated to the values in $\mathcal{T}_n$.

As a result of Algorithm 1, we have a list of Candidate Source Points (CSP) which represents a first estimation of S. This first estimate will be denoted as S^0. Figure 3 shows two outputs of Algorithm 1. In both examples two PMJs, represented by stars, are shown. The set of red circles corresponds to the estimated CSPs, generated from the measurement points (small crosses). The figures show that Algorithm 1 gives a resulting list with many false positives. From Eq. (4), it can be seen that for a point $\mathbf{x}$ that is near a source point $\mathbf{s}$, the terms involving distance are similar in magnitude and will almost cancel each other. As a consequence, points that are near to source points are also likely to be detected as such.

To reduce the number of false positives, we apply a second step, described in Algorithm 2. Starting from $listCSP$, we process the points again to remove spurious points and obtain a more accurate set of PMJs. In this second step, every CSP in S^0 is given a score that is intended to assign high values to actual PMJs and low values to spurious ones. The function we use to score the candidates is $-t(\mathbf{x})$. The motivation for this function is that PMJs are activated through the Purkinje network, where propagation speed is faster than in working myocardium and, as a consequence, CSPs with a later activation time are more likely to be false estimates. Therefore, the set of CSPs is ordered according to this score so that we first assess the elimination of those points with lower score value (higher activation time). For each point, we evaluate if the resulting set S still explains the observed activation properly, that is with similar or lower error.

We start the second step of the method by computing the estimated t_i of every measurement point $\mathbf{p} \in \mathcal{P}$ using equation (1). This t_i is computed using the estimated sources, and allows us to assign to every CSP the list of the measurement points it has
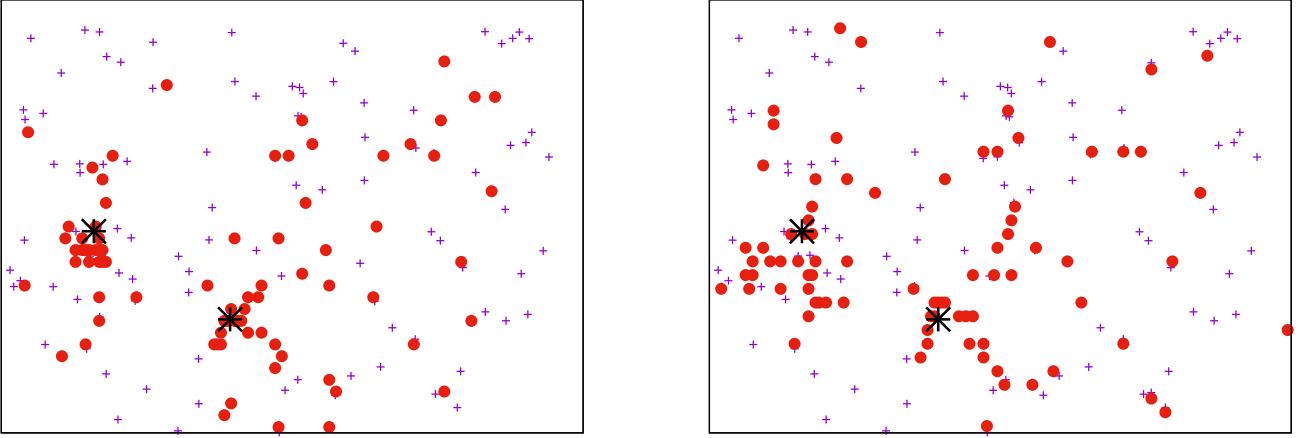
FIGURE 3 Candidate Source Points (red circles) after the application of Algorithm 1 for two real sources (stars) with a deviation in the error of 0.5ms (Left) and 1.5ms (Right). Measurement points are represented with small crosses. The signal propagates from the lower left corner of the image to the upper right corner. It can be observed that spurious candidate sources appear, specially near the actual source points.

activated. The value of the score is also computed for every CSP (line 1 of Algorithm 2, in $CalculateScore$). Then, we take the CSP, $\mathbf{x} \in S^0$, with the lowest score value, we remove $\mathbf{x}$ from the set S^0 and try to reassign the set of points it activated, $A(\mathbf{x})$, as follows. Given a point $\mathbf{p}_i \in A(\mathbf{x})$, we consider $\mathbf{s} \in S^0$, with $\mathbf{s} \neq \mathbf{x}$, and we take the backwards electrical propagation $a_i(\mathbf{s})$ that was computed in the first step of the method. We compute the distance from $a_i(\mathbf{s})$ to the estimated activation time $\delta_{i,\mathbf{s}} = |t(\mathbf{s}) - a_i(\mathbf{s})|$. For every point $\mathbf{p}_i \in A(\mathbf{x})$, we will say that it *can be reassigned* to source $\mathbf{s}$ if $\delta_{i,\mathbf{s}} \leq \beta\sigma$, where $\beta > 0$ is a parameter that determines how restrictive we are to allow a point to be reassigned. Once this information has been computed for all the measurement points, we will establish that the candidate $\mathbf{x}$ can be removed if all the points in $A(\mathbf{x})$ can be reassigned to another source in $S^0 - \{\mathbf{x}\}$. This evaluation is performed by procedure $CanBeReassigned$ in line 5 of Algorithm 2, returning true only if all the points in $A(\mathbf{x})$ can be reassigned within the tolerance defined by parameter β. The method $Reassign$ in line 6 takes the measurement points in $A(\mathbf{x})$ and reassigns them to the best remaining candidate sources in the list. If the point $\mathbf{x}$ cannot be removed, then it is inserted again in S^0. This process is repeated for all the CSPs, in increasing order of the score. Once this process is completed for all the points $\mathbf{x} \in S$, we will have a new set of estimated source points, $S^1 \subseteq S^0$. The complete process is repeated to build a sequence of estimations $S^0 \supseteq S^1 \supseteq \cdots \supseteq S^k$ until we reach an iteration in which $S^k = S^{k+1}$, which means that no point in S^k can be removed. The set of source points resulting from this process, S^k, is taken as the final estimation of S. This process can also be stopped after a fixed number of iterations. Indeed, according to our experiments, most of the CSP removal is done in the first iteration.

2.3 | Experiments

We have set up a series of experiments to test the proposed methodology. We start our evaluation with a simplified scenario where we consider an Euclidean 2-dimensional domain. To test the methodology in a realistic scenario, we use a 3-dimensional model of the left ventricular endocardium that includes different complex computer generated Purkinje networks. The ventricular mesh has been obtained from a virtual population of segmented hearts built from medical imaging of real patients (30). The human ventricular model has the following dimensions: 8.65 cm (long axis) x 5.22 cm (short axis). The endocardial mesh, where the Purkinje networks are deployed, is made of 42144 triangular elements and 21189 nodes.

2.3.1 | Experiments on Euclidean, 2-dimensional scenarios

The set of 2-dimensional planar scenarios reproduce those used in (27) to test the algorithm presented therein to estimate a set of PMJ from measured data. In that work, LATs were free of error. The main goal of this test is to evaluate the performance of the new method proposed here, compared to the algorithm in (27) applied to noise free data.
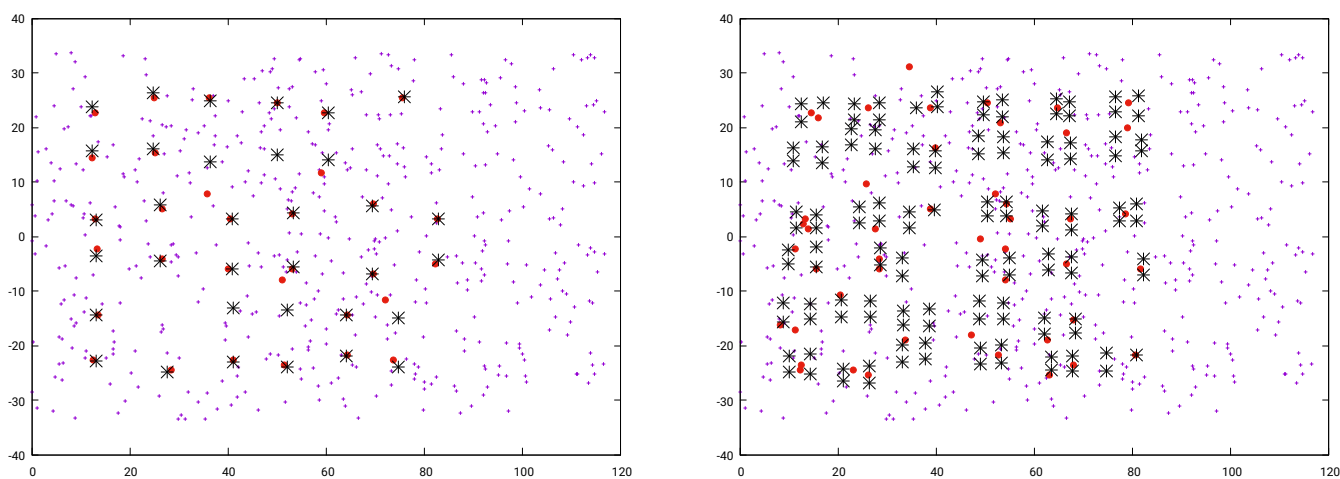

Algorithm 2 CSP reduction

1: $listCSP2 \leftarrow CalculateScore(listCSP)$
2: **repeat**
3:     $changed \leftarrow False$
4:     **for all** $(\mathbf{x}, A(\mathbf{x})) \in listCSP2$ **do**
5:         **if** $(CanBeReassigned(A(\mathbf{x}), listCSP2 - \{\mathbf{x}\})$ **then**
6:             $Reassign(A(\mathbf{x}), listCSP2)$
7:             $listCSP2 \leftarrow CalculateScore(listCSP2)$
8:             $changed \leftarrow True$
9:         **end if**
10:     **end for**
11: **until** $not(changed)$
12: **Output** $\leftarrow listCSP2$

FIGURE 4 2-dimensional scenarios with random set of measurement points (small crosses), real sources (stars) and location of estimated source points (red circles). Standard deviation in the measurement error of 0.5ms. Left: Example of B3D2 scenario with 34 PMJs. Right: Example of B3D4 scenario with 130 PMJs. Units are in mm.

In these tests, the scenarios are rectangular regions with an area similar to that of a human left ventricle, and we use simplified versions of a PKN in the ventricle, based on a binary tree. The trees are built randomly by creating a number of main branches, and building ramifications of this branch up to a given depth d. A higher value of d leads to more PMJs distributed around the main branch. The trees have been built using four different configurations, with ten random trees of each type. Two of the configurations have a single main branch, and use depth $d = 2$ and $d = 4$ in the sub-branch generation. The other two configurations consider three main branches, spanning parallel to each other, and with the same values for d. In Figure 4 two of the scenarios are shown: B3D2 with 34 PMJs and B3D4 with 130 PMJs. For further details on the procedure to build the different tree models see (27).

2.3.2 | Experiments on 3-dimensional human ventricles

The second set of tests is performed on a left ventricular mesh generated from a virtual population constructed from a set of segmented medical images. On these 3-dimensional models we built synthetic PKNs using the stochastic method described by (10). A total of 20 different scenarios with diverse PKN morphology, number of PMJ (varying from 213 to 1228), and heterogeneity in PMJ density were built. These scenarios will be referred to as PK1,..., PK20. The activation maps generated by Purkinje trees built with this method were already validated in (10), by analyzing the activation sequence and the total activation
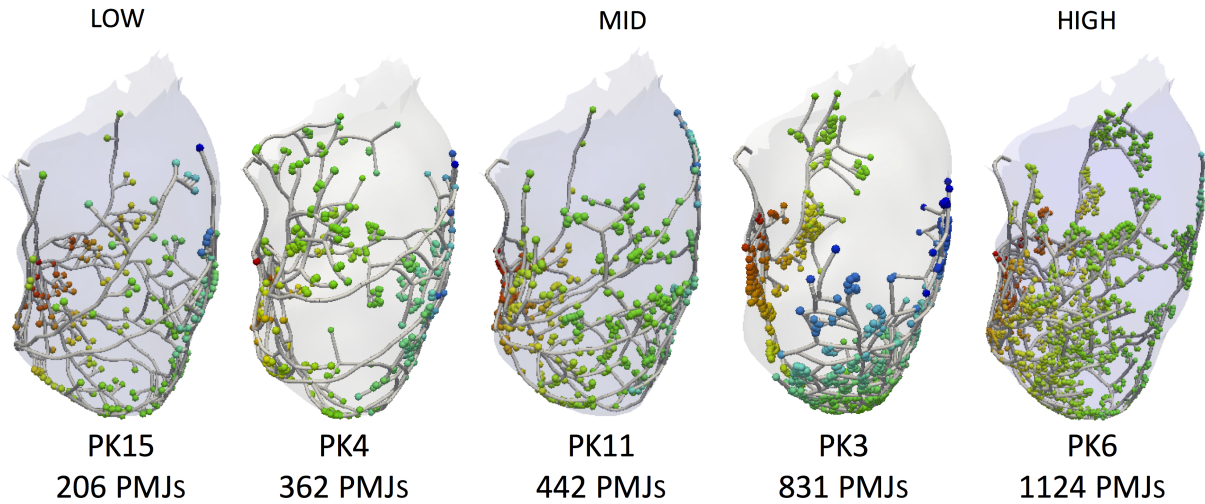
FIGURE 5 Purkinje tree models developed with an increasing number of PMJs and PMJ density. As can be observed the distance between PMJs is lower in PK3 and PK6.

times. Figure 5 shows the structure and location of PMJs for three different PKNs with low, medium and large amount of PMJs. The real LAT for the PMJs was calculated considering the activation of atrio-ventricular node at $t = 0ms$ and a constant conduction velocity in the PKN of $3m/s$.

For each scenario we studied the effect of the number of measurement points by placing different sets with an increasing density (100, 250, 500, 1000, 1500 and 2000) uniformly distributed as in a real EAM acquisition. To make the results independent of the measurement point locations, for each set size we randomly sampled (Mersenne twister random engine) the endocardium 10 different times. Results are provided for the average of the 10 different sampling sets. The correct LATs for these measurement points are calculated propagating a signal from the PMJs to all the computational nodes in the domain, by solving the isotropic Eikonal equation using a fast marching algorithm (29). Once the actual LAT for each measurement point is known, we add Gaussian noise to the LAT as described in section 2.1, with a mean of 0 and a standard deviation ranging from 0 ms to 5.0 ms (in particular: 0ms, 0.5ms, 1.5ms, 2.5ms and 5.0ms).

In order to measure the quality of estimated PMJ sets we use two main indicators. First, we compare the activation map generated by propagating the electrical signal from the estimated PMJs to the real activation map, at all the nodes of the computational mesh (21189 nodes). We take the absolute value of the difference in the activation time at every mesh node as the error at that point, and measure the error of the activation map as the mean absolute error over all the points in the mesh. As a second quality indicator, we consider the distance from each estimated PMJ to the closest real PMJ. This distance indicates if the method has located a false estimated PMJ far from the actual Purkinje tree. This situation is indicated by the appearance of large values of this error measure.

3 | RESULTS AND DISCUSSION

The method proposed has been applied to the synthetic 2-dimensional scenarios described in Section 2.3.1. A set of 1000 measurement points have been generated with a uniform random distribution on the simulation region, and Gaussian noise has been added to the computed LATs. The tests have been repeated for different values of standard deviation σ^2.

Table 1 shows the results obtained for the different types of trees, considering the number of main branches and bifurcation depth. The table shows the average results for the 10 synthetic Purkinje trees built using the same parameters. The first column indicates the tree configuration. In the labels, the number alongside label B indicates the number of main branches and the number following label D the depth of the ramification. The second column indicates the average number of PMJs in that configuration. The following columns show the results for two magnitudes of the measurement error; $\sigma = 0.5$ and $\sigma = 2.5$. For each value of σ, the first column indicates the average number of estimated PMJs that are found by the algorithm, the second

Scenario		Gaussian Error 0.5			Gaussian Error 2.5		
Num.	PMJ	Est. PMJ	Abs. Error(ms)	D. Fe-F(mm)	Est. PMJ	Abs. Error(ms)	D. Fe-F(mm)
B1D2	11.7 ± 0.5	18 ± 3	0.22 ± 0.07	0.34 ± 0.05	16 ± 3	1.02 ± 0.48	1.72 ± 0.32
B1D4	43.9 ± 2.5	42 ± 4	0.33 ± 0.05	1.11 ± 0.16	17 ± 3	1.12 ± 0.33	3.31 ± 0.31
B3D2	35.4 ± 0.9	40 ± 3	0.28 ± 0.03	1.52 ± 0.24	25 ± 3	1.21 ± 0.18	4.49 ± 0.39
B3D4	132.2 ± 3.6	68 ± 5	0.46 ± 0.04	2.71 ± 0.16	25 ± 3	1.29 ± 0.14	5.25 ± 0.32

TABLE 1 Results for 2-dimensional scenarios with 1000 measurement points and Gaussian noise with a standard deviation of $\sigma = 0.5$ms and $\sigma = 2.5$ms. Column *Num* identifies the scenario, *PMJs* represents the number of PMJs in the scenario, *Est. PMJs* is the number of estimated PMJs by the algorithm, *Abs. Error* is the mean of the absolute error in all the points of the mesh and *D. Fe-F* is the distance from an estimated PMJs to the nearest real PMJ.
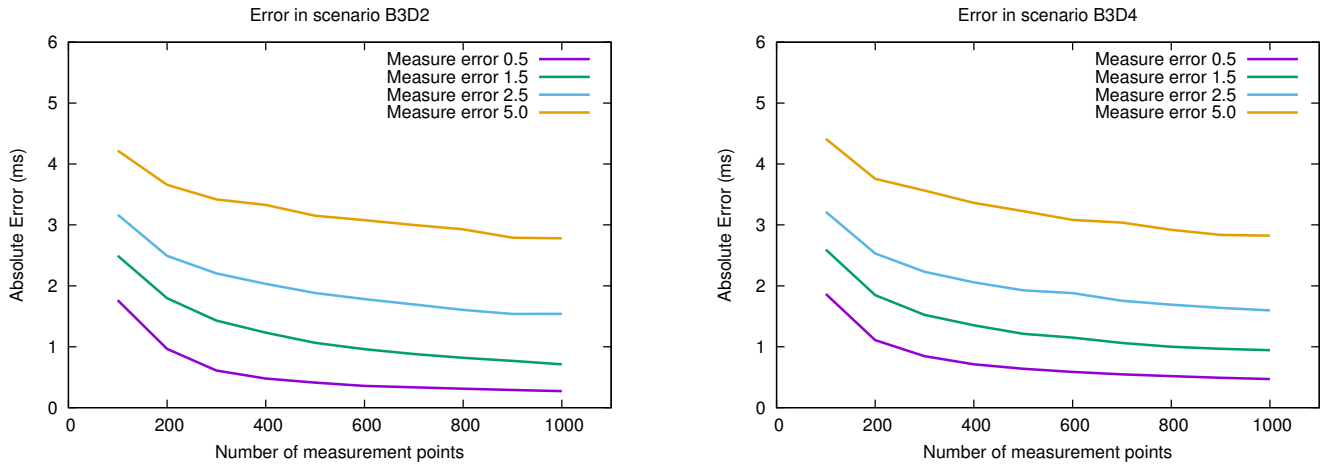
FIGURE 6 Absolute error for scenarios B3D2 and B3D4 with different number of measurement points and a standard deviation error in the measurement of 0.5, 1.5, 2.5 and 5.0 milliseconds.

column indicates the average absolute error of the resulting activation map and the third column shows the maximum distance from the estimated PMJs to the real ones.

Figure 6 shows the evolution of the mean absolute error for the scenarios B3D2 and B3D4 when changing the number of measurement points (size of input data). From the results we can see that errors are kept low independently of the number of measurement points. Moreover, although the error grows as σ increases, observed errors are always lower than the standard error introduced in the samples, even for just 100 measurement points in some cases. It is noteworthy that the number of measurements is often over 500 in real acquisitions during catheter ablation interventions. These results improve the errors obtained in our previous work (27) which, despite the absence of error, were larger for all the number of measurement points analyzed. The results for $\sigma > 0$ cannot be compared, since the method in the previous work was not able to handle error in the measurement data, and the errors grew as σ was increased. However, results in (27) show absolute errors larger than $10ms$ for sets with less than 200 measurement points, while the new method can obtain absolute errors below $4ms$ even in presence of errors of $0.5ms$ in the samples. In addition, it converges to values below $0.5ms$ in absolute error when the number of samples increases.

The study in 3-dimensional ventricles focused on the estimation of PMJs from 20 distinct synthetic PKN. A summary of the different PKN properties, including number of PMJs, and mean density and standard deviation of PMJs per segment (17 AHA segment division), can be seen in table 2 , and table S1 in Supplementary Material. For each PKN configuration, the corresponding LAT map was generated by firstly simulating the signal propagation on the tissue, and secondly randomly sampling (as in a real EAM) the endocardium using an increasing amount of measurement points to study the effect of the sampling density on the results accuracy. Since the endocardial sampling was random, each sampling size was repeated 10 times for each configuration, and results were averaged. Finally, we introduced Gaussian noise in all the samples with different standard deviations. As a result of all the combinations we obtained 6000 different scenarios for which PMJs were estimated. Table 3 (the

full set of results is summarized in S1 Table in Supplementary Material) summarizes the average results for six selected PKN using 1000 measurement points, which is a feasible amount for an EAM, and two different levels of Gaussian noise ($\sigma = 0.5ms$ and $\sigma = 2.5ms$). Note that clinical studies that use contact-mapping catheter systems such as (31) (CARTO3, Webster BioSense Inc.), or non-contact-mapping catheters (32) (Rhythmia mapping, Boston Scientific) have reported that they could collect 1000 measurement points (3-5 minutes), and 4227 measurement points (6.1 minutes), respectively.

When we introduced Gaussian noise with a standard deviation of $0.5ms$ in the measurements, the absolute LAT error obtained in the estimated PMJs for the whole mesh ranged between $0.5ms$ and $0.9ms$. The average distance from the estimated PMJs to the real PMJs (D. Fe-F) ranged from 1.1mm to 1.5mm. This means that the algorithm finds the more influential PMJs and only a small number of estimations do not correspond to real ones. Figure 7 shows the estimation results for PK15, which includes 206 PMJs. Real PMJs are represented by circles, while estimated PMJs are displayed as squares. When PMJs are not clustered, the algorithm matches their location with high accuracy. In regions with clustered PMJs, some representative PMJs are detected, that summarize the whole activity in the area. In Figure 7 detail, it can be observed that incorrectly estimated non-existent PMJs produce an early activation in the region (label '1', bluish colours), while missing the detection of a PMJs produces a late activation in the region (label '2', redish colours). However, most of the PMJs are correctly estimated, and therefore when activation is triggered from estimated PMJs the error in the mesh is close to 0. For Gaussian noise with a standard deviation of $2.5ms$ the absolute errors obtained in the mesh were still low, around 1.7ms in average, specially when compared with the deviation in the measurement introduced. However, the distance error clearly increased with values ranging from 1.9mm to 4.0mm. As we increased errors in the measurements, there was an increasing possibility of estimating erroneous PMJs.

In Figure 8 we have a representative selection of the scenarios visualized in 3D where the surface meshes are colour-coded with the absolute LAT error on the mesh, that is the difference between the real LAT and the new LAT calculated from the estimated PMJs. As can be observed in the first row (measurement error of 0.5ms) almost all meshes show a local error in the range of -2ms to 2ms. In the second row (measurement error of 2.5ms) local errors increased in several areas, where both false and underestimated PMJs occurred. In blue colour we have regions that were activated too early by the estimated PMJs, and in red colour areas that were activated later than ground truth. Among the reasons that produced the underestimation there is the lack of measurement points in certain areas due to the random mapping, or the summarization in groups of PMJs detected by the algorithm. On the other hand, false PMJs were added because several CSPs belonging to the same source were not correctly merged in the second step of the method due to an excessive error in the measurement points. The creation of an excessive number of false PMJs can be controlled increasing the parameter β commented in section 2.2, but then more PMJs will be clustered together.

The plots in Figure 9 show the variation of the absolute LAT error as we increase the number of measurement points with different levels of Gaussian noise. We can observe that in general, the absolute error decreases with more measurement points except when the Gaussian noise introduced in the measurements is too high. With Gaussian noise with a standard deviation of 5.0ms, the absolute error increases with the number of measurement points, due to the inclusion of spurious PMJs in the estimated set. This clearly represents a limit in the error admitted by the actual algorithm. We can also see in the plots that in the scenarios with a low density of PMJs and with small deviations in the error, the absolute LAT error tends to zero. The plots in Figure 10 show the variation in the distance from estimated PMJs to real PMJs for the same scenarios. In these plots we observe that for small standard deviations (0.0ms and 0.5ms) in the measurement error, the mean distance between real and estimated PMJs decreases as we increase the number of measurement points. However, when higher errors in the measurement points ($> 1.5mm$) are introduced, the number of measurement points do not always improve the results. That means that with more error, we estimate PMJs in erroneous positions. We can also notice that the density of PMJs does not have a clear effect in these plots. The distance from estimated PMJs to real PMJs seems to depend more on the geometry of the Purkinje tree than on the number of PMJs.

Other authors have presented in the past algorithms to set the activation sequence of the ventricles using different techniques, but only a few of them are based on clinical data or other types of ground truth data to compare with. The two most common non-personalized approaches are the manual inclusion of endocardial activation triggers in accordance with descriptions in the literature (33), or the generation of synthetic Purkinje trees without a specific patient reference. The latter approach has been performed with different mathematical techniques that range from simple fractal trees (34) to complex and dense network structures based on L-systems (10). Another method is based on segmentation of the proximal section of the PKN from ex-vivo biological (35, 12, 36, 13), but PMJs cannot be obtained, except at a few specific locations (15). However, all those strategies are valid for mechanistic studies, and do not allow to generate patient-specific activation sequences or ECGs, such as those presented in our work. EAM data have been used in different ways to estimate the PKN to subsequently perform simulations

|	Scenario			
Num.	PMJ	Density	TAT pkj (ms)	TAT (ms)
PK1	1128	94.1 ± 0.7	10.0	51.5
PK3	831	51.9 ± 1.1	15.6	47.4
PK4	362	22.6 ± 0.7	12.7	35.1
PK6	1224	76.5 ± 0.7	11.3	33.0
PK11	442	27.6 ± 0.6	12.8	34.5
PK15	206	14.7 ± 0.6	13.5	35.5

TABLE 2 Information about six representative 3-dimensional scenarios. Column *Num* identifies the scenario, *PMJ* represents the number of PMJs in the scenario, *Density* is the density and standard deviation of PMJs per segment (17 AHA segment division), *TAT pkj* is the Total Activation Time of the Purkinje Network, *TAT* is the Total Activation Time for the whole surface/ventricle.

Scenario		Gaussian Error 0.5				Gaussian Error 2.5			
Num.	PMJ	Est. PMJ (%)		Abs. Error(ms)	D. Fe-F(mm)	Est. PMJ (%)		Abs. Error(ms)	D. Fe-F(mm)
PK1	1128	91 ± 4	(8.0)	0.69 ± 0.03	1.19 ± 0.19	53 ± 3	(4.7)	1.64 ± 0.16	3.37 ± 0.76
PK3	831	95 ± 3	(11.4)	0.67 ± 0.03	1.16 ± 0.11	56 ± 5	(6.8)	1.63 ± 0.14	2.71 ± 0.41
PK4	362	103 ± 4	(28.3)	0.68 ± 0.04	1.34 ± 0.15	62 ± 3	(17.0)	1.74 ± 0.13	2.84 ± 0.18
PK6	1224	116 ± 2	(9.5)	0.82 ± 0.03	1.08 ± 0.03	62 ± 5	(5.0)	1.74 ± 0.10	1.92 ± 0.27
PK11	442	108 ± 3	(24.5)	0.75 ± 0.04	1.41 ± 0.13	63 ± 3	(14.2)	1.74 ± 0.11	2.58 ± 0.33
PK15	206	86 ± 4	(41.6)	0.60 ± 0.04	1.34 ± 0.15	53 ± 4	(25.8)	1.67 ± 0.10	3.21 ± 0.33

TABLE 3 Results for six representative 3-dimensional scenarios with 1000 measurement points and Gaussian noise with standard deviation of 0.5 and 2.5. Column *Num* identifies the scenario, *PMJs* represents the number of PMJs in the scenario, *Est. PMJs* is the number of estimated PMJs by the algorithm, *Abs. Error* is the mean of the absolute error in all the points of the mesh and *D. Fe-F* is the distance from an estimated PMJs to the nearest real PMJ.

of cardiac electrophysiology. In (25) PMJs were obtained from EAMs, previously fit to a reference endocardial model, by calculating sources and sinks from the patient LAT maps. The method used not only the data at the measurement points but all the interpolated information on the mesh, which probably introduced errors in the estimation since the interpolation does not reflect the real activation sequence. LAT errors reported ranged from 5.12 ms to 8 ms. In (23, 26), during the validation analysis, the estimation of PMJs was performed considering previously a synthetic PKN structure, and following moving, adding or deleting PMJs to decrease the error with respect to measurements. The main similarity of our method with the one presented in (26) is that both use the solution of the backward Eikonal equation (from the measurement points to the points in the mesh) to search for (or move/add/delete) candidate PMJs. However, the criterion we define to decide the final PMJs is different to that in (26). In addition, in our methodology we consider that the samples include Gaussian noise due to the annotation of the measurement points. Finally, in (26) the optimization of the PMJ locations is done per *region of interest* while the method presented here uses a global ranking of the candidate PMJs. In (23), the authors reported mean absolute errors ranged from 4.9 ± 4.1 ms to 9.9 ± 7.5 ms, depending on the subject and the initial PKN, whereas in (26), results were improved significantly. It is important to remark that in both studies patient-specific electro-anatomical data were used. For synthetic PKN without noise in the samples, the mean absolute error for 300 measurement points ranged from 1.92 ± 2.00ms to 2.94 ± 2.82 ms depending on the number of test points used for the cross-validation. For an equivalent number of measurement points without noise, we obtained mean absolute errors of around 1*ms* using a cross-validation with 21189 points (i.e. all the endocardial points). With regard to the results including noise, the comparison is difficult since the noise was included in a different way, and we cannot determine which is the equivalent noise between both studies. Finally, in (26) EAMs were used to test the methodology, and results show mean absolute errors of 5.84 ± 4.45 ms for the patient-specific network. Although we do not have results yet for acquired EAMs, these results serve as a reference to indicate that our errors with synthetic EAMs are below these values.

One of the drawbacks of using a previously defined PKN structure, as in (23, 26), is that this imposes a constraint for the location and amount of the PMJs. Thus starting with an inaccurate PKN can affect the quality of the final estimation of the set of
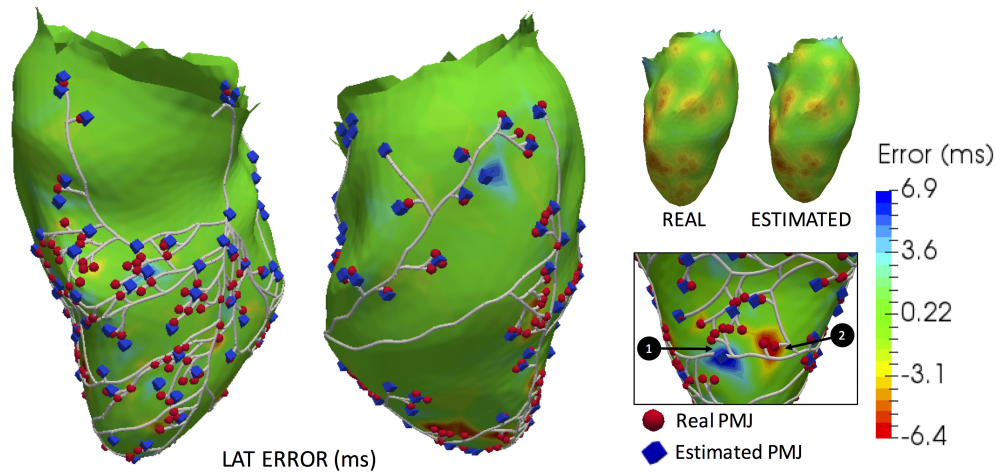
FIGURE 7 Estimation in low PMJ density model. Left panel shows two views of the endocardium where colour correspond to the error in ms between the real LAT and the estimated LAT. LATs obtained with real PMJs and estimated PMJs is depicted in the upper row. A detail of an endocardial region is provided, including real (circles) and estimated (squares) PMJs. Red areas (label 2) correspond to errors where PMJs have not been detected and activation is delayed, while blue areas (label 1) correspond to wrongly estimated PMJs, which activate tissue too early.

PMJs. On the contrary, our approach works directly with the estimation of PMJs locations, which are completely free from any predefined PKN structure. It is also important to remark than only a few studies such as (26) have explicitly considered errors in the clinical measurements. That is relevant, since mapping systems have been reported to introduce errors in the catheter tip position of about 0.7 ± 1.5 mm (37), which have to be added to the errors due to the LAT annotation from the monopolar and bipolar catheter recordings.

So far, there has not been a thorough analysis of the density of Purkinje myocardial junctions in the human heart. There have been a few attempts to describe PMJs in selected regions of the heart such the base of the papillary muscles, or random locations, in a few hearts. Most of the studies that analyze the PK system and PMJs have been carried out in animals, which present a different configuration than in humans. Therefore, applying techniques to estimate the density of PMJs to a large number of human cases can shed some light in the distribution and density of them, allowing to build atlases.

4 | CONCLUSIONS

We have presented a methodology to estimate the sources of electrical activation in the ventricles, that in normal conditions will correspond to PMJs hotspots. From the electrical information recorded with an electro-anatomical mapping system at discrete locations, the method could provide the location and activation times of the electrical triggers with an error bounded by the measurement system error. The errors in location and activation times obtained are small enough to permit the accurate simulation of sequences of activation in biophysical models of cardiac electrophysiology. In areas where a large number of PMJs exist, the system would recover a representative set of source points that can predict the combined effect of all the real PMJs with a low absolute error. Non-clustered PMJs can be located with high precision, even when LAT errors are incorporated in the samples. Finally, the number of endocardial electrical samples required by the method is well within standard clinical EAM procedures, which makes it more applicable. We consider that widely used electro-anatomical mapping systems such as CARTO3 (Biosense Webster, Inc), Ensite NavX (St. Jude Medical), or the new Rhythmia system (Boston Scientific), can acquire more than 1000 samples in times that are compatible with an intervention in the EP lab. The location of the PMJs could be useful to reproduce the activation sequence of a given patient in the model, or to plan radiofrequency ablation therapies that target the PMJs to stop a macro-reentrant tachycardia. One of the drawbacks of the model is that it requires a few parameters such as the system measurement error, which is the sum of the error location and the automatic LAT annotation. This information, however, can often be retrieved from the manufacturer of the EAM device used. In addition, the method has to be applied to a
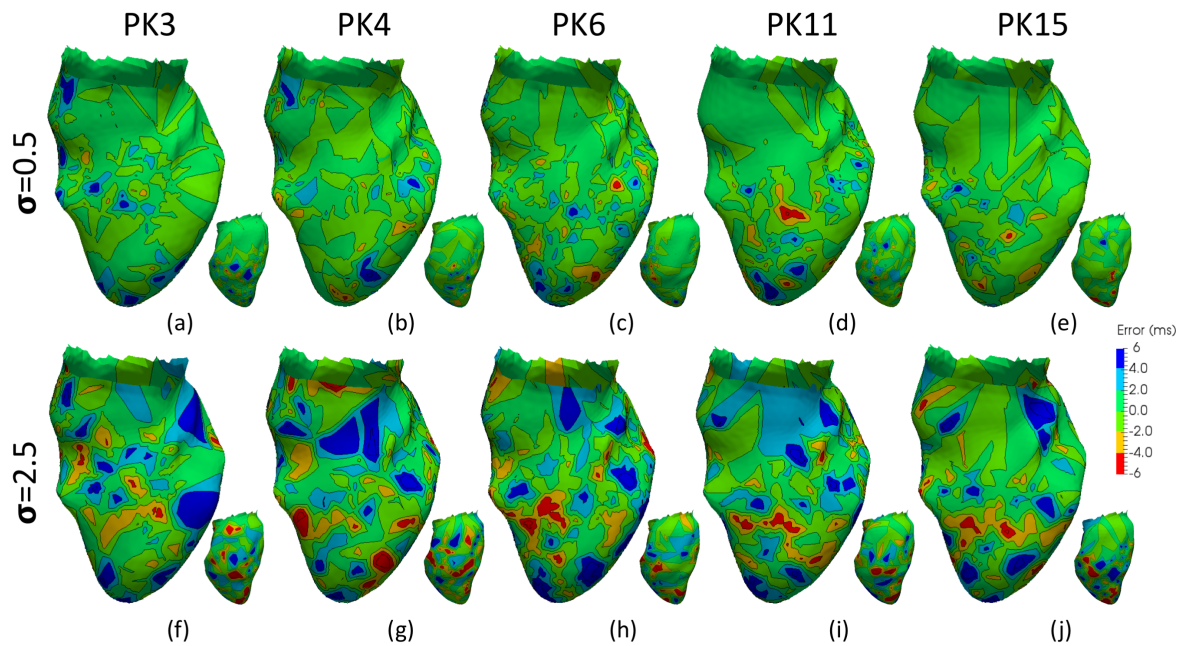
FIGURE 8 Spatial distribution of LAT errors. Local differences in activation times between simulations triggered from real and estimated PMJs. Five different Purkinje tree configuration with differences in PMJ density (see Table 3) for which Gaussian noise with standard deviation $\sigma = \{0.5, 2.5\}$ were included in the samples. Errors are colour coded using a scale bar between -6.0ms and 6.0ms. Red colours mean that estimated map activated later than real, and blue colours that estimated map activated earlier.

large cohort of patient specific EAMs in order to analyze the distribution of PMJs in real cases, and not only in simulated data, to draw meaningful clinical conclusions. Finally, the current model only retrieves the PMJs, and not the CCS branching structure. A complete CCS would be required to model pathologies such as bundle branch block, macro-reentries that involve the Purkinje system, or treatments such as cardiac resynchronization therapy.

ACKNOWLEDGEMENTS

References

[1] Trayanova Natalia A, Chang Kelly C. How computer simulations of the human heart can improve anti-arrhythmia therapy. *J Physiol.* 2016;594(9):2483-502.

[2] Arevalo Hermenegild J, Boyle Patrick M, Trayanova Natalia A. Computational rabbit models to investigate the initiation, perpetuation, and termination of ventricular arrhythmia. *Prog Biophys Mol Biol.* 2016;121(2):185-94.

[3] Lopez-Perez Alejandro, Sebastian Rafael, Ferrero Jose M. Three-dimensional cardiac computational modelling: methods, features and applications. *Biomed Eng Online.* 2015;14:35.

[4] Deng Dongdong, Arevalo Hermenegild J, Prakosa Adityo, Callans David J, Trayanova Natalia A. A feasibility study of arrhythmia risk prediction in patients with myocardial infarction and preserved ejection fraction. *Europace.* 2016;18(suppl 4):iv60-iv66.

[5] Dux-Santoy Lydia, Sebastian Rafael, Felix-Rodriguez Jose, Ferrero Jose Maria, Saiz Javier. Interaction of specialized cardiac conduction system with antiarrhythmic drugs: a simulation study. *IEEE Trans Biomed Eng.* 2011;58(12):3475-8.
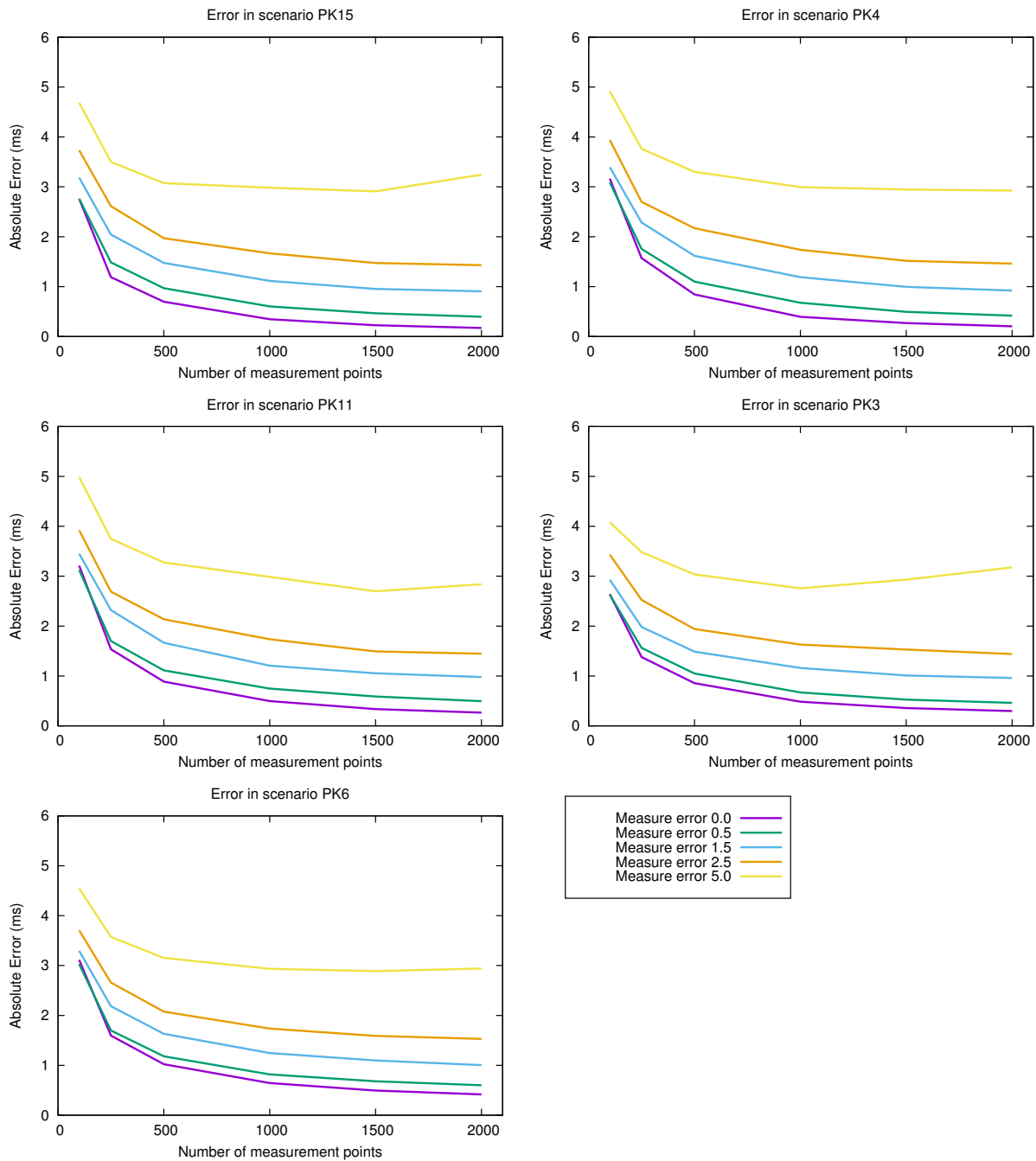
FIGURE 9 Plots of the absolute error for 5 different scenarios in increasing order of PMJs density: PK15, PK4, PK11, PK3 and PK16.

[6] Sanchez-Quintana D, Garcia-Martinez V, Climent V, Hurle J M. Morphological changes in the normal pattern of ventricular myoarchitecture in the developing human heart. *Anat Rec.* 1995;243(4):483-95.

[7] Jeffery Nathan S, Stephenson Robert S, Gallagher James A, Jarvis Jonathan C, Cox Philip G. Micro-computed tomography with iodine staining resolves the arrangement of muscle fibres. *J Biomech.* 2011;44(1):189-92.

[8] Streeter D D, Spotnitz H M, Patel D P, Ross J, Sonnenblick E H. Fiber orientation in the canine left ventricle during diastole and systole. *Circ Res.* 1969;24(3):339-47.
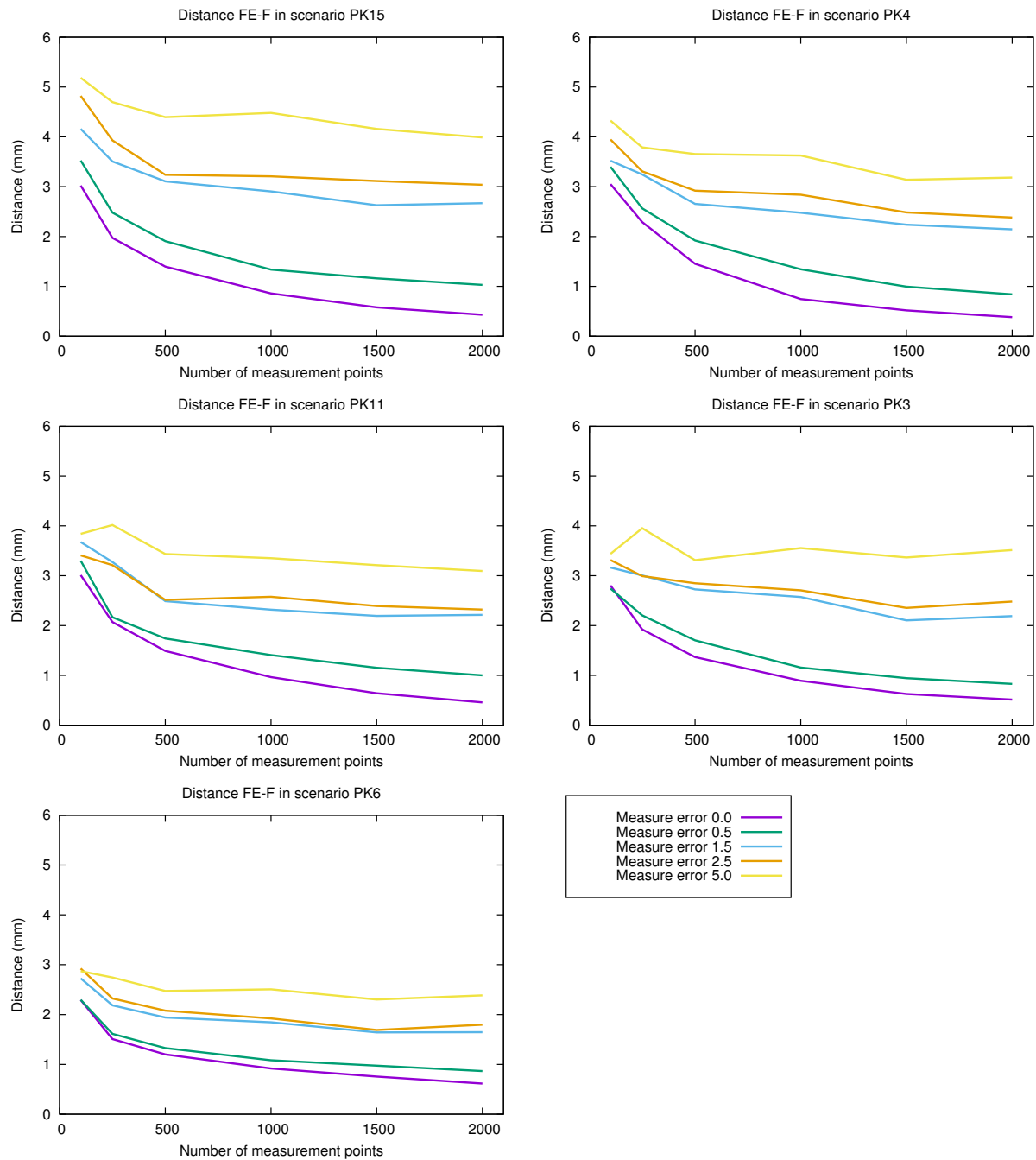
FIGURE 10 Plots of the distance from estimated PMJs to real PMJs for 5 different scenarios in increasing order of PMJs density: PK15, PK4, PK11, PK3 and PK16.

[9] Pashakhanloo Farhad, Herzka Daniel A, Mori Susumu, et al. Submillimeter diffusion tensor imaging and late gadolinium enhancement cardiovascular magnetic resonance of chronic myocardial infarction. *J Cardiovasc Magn Reson.* 2017;19(1):9.

[10] Sebastian Rafael, Zimmerman Viviana, Romero Daniel, Sanchez-Quintana Damian, Frangi Alejandro F. Characterization and modeling of the peripheral cardiac conduction system. *IEEE Trans Med Imaging.* 2013;32(1):45-55.

[11] Vigmond Edward J, Stuyvers Bruno D. Modeling our understanding of the His-Purkinje system. *Prog Biophys Mol Biol.* 2016;120(1-3):179-88.

[12] Stephenson Robert S, Boyett Mark R, Hart George, et al. Contrast enhanced micro-computed tomography resolves the 3-dimensional morphology of the cardiac conduction system in mammalian hearts. *PLoS One.* 2012;7(4):e35299.

[13] Stephenson Robert S, Atkinson Andrew, Kottas Petros, et al. High resolution 3-Dimensional imaging of the human cardiac conduction system from microanatomy to mathematical modeling. *Sci Rep.* 2017;7(1):7188.

[14] Romero Daniel, Camara Oscar, Sachse Frank, Sebastian Rafael. Analysis of Microstructure of the Cardiac Conduction System Based on Three-Dimensional Confocal Microscopy. *PLoS One.* 2016;11(10):e0164093.

[15] Garcia-Bustos V, Sebastian R, Izquierdo M, Molina P, Chorro F J, Ruiz-Sauri A. A quantitative structural and morphometric analysis of the Purkinje network and the Purkinje-myocardial junctions in pig hearts. *J Anat.* 2017;230(5):664-678.

[16] Behradfar Elham, Nygren Anders, Vigmond Edward J. The role of Purkinje-myocardial coupling during ventricular arrhythmia: a modeling study. *PLoS One.* 2014;9(2):e88000.

[17] Nogami Akihiko. Purkinje-related arrhythmias part I: monomorphic ventricular tachycardias. *Pacing Clin Electrophysiol.* 2011;34(5):624-50.

[18] Reithmann Christopher, Hahnefeld Anton, Oversohl Nico, Ulbrich Michael, Remp Thomas, Steinbeck Gerhard. Reinitiation of ventricular macroreentry within the His-Purkinje system by back-up ventricular pacing - a mechanism of ventricular tachycardia storm. *Pacing Clin Electrophysiol.* 2007;30(2):225-35.

[19] Haissaguerre Michel, Vigmond Edward, Stuyvers Bruno, Hocini Meleze, Bernus Olivier. Ventricular arrhythmias and the His-Purkinje system. *Nat Rev Cardiol.* 2016;13(3):155-66.

[20] Romero Daniel, Sebastian Rafael, Bijnens Bart H, et al. Effects of the purkinje system and cardiac geometry on biventricular pacing: a model study. *Ann Biomed Eng.* 2010;38(4):1388-98.

[21] Boyden Penelope A, Dun Wen, Robinson Richard B. Cardiac Purkinje fibers and arrhythmias; The GK Moe Award Lecture 2015. *Heart Rhythm.* 2016;13(5):1172-81.

[22] Teng Alexandra E, Lustgarten Daniel L, Vijayaraman Pugazhendhi, et al. Usefulness of His Bundle Pacing to Achieve Electrical Resynchronization in Patients With Complete Left Bundle Branch Block and the Relation Between Native QRS Axis, Duration, and Normalization. *Am J Cardiol.* 2016;118(4):527-34.

[23] Vergara Christian, Palamara Simone, Catanzariti Domenico, et al. Patient-specific generation of the Purkinje network driven by clinical measurements of a normal propagation. *Med Biol Eng Comput.* 2014;52(10):813-26.

[24] Palamara Simone, Vergara Christian, Catanzariti Domenico, et al. Computational generation of the Purkinje network driven by clinical measurements: the case of pathological propagations. *Int J Numer Method Biomed Eng.* 2014;30(12):1558-77.

[25] Cárdenes Rubén, Sebastian Rafael, Soto-Iglesias David, Berruezo Antonio, Camara Oscar. Estimation of Purkinje trees from electro-anatomical mapping of the left ventricle using minimal cost geodesics. *Med Image Anal.* 2015;24(1):52-62.

[26] Palamara Simone, Vergara Christian, Faggiano Elena, Nobile Fabio. An effective algorithm for the generation of patient-specific Purkinje networks in computational electrocardiology. *Journal of Computational Physics.* 2015;283(Supplement C):495 - 517.

[27] Barber Fernando, Lozano Miguel, Garcia-Fernandez Ignacio, Sebastian Rafael. Inverse Estimation of Terminal Connections in the Cardiac Conduction System. *Mathematical Methods in Applied Sciences.* 2018;41(6):2340-2349.

[28] Keener J P. An eikonal-curvature equation for action potential propagation in myocardium. *J Math Biol.* 1991;29(7):629-51.

[29] Sethian J. A.. Fast Marching Methods. *SIAM Review.* 1999;41(2):199-235.

[30] Hoogendoorn Corné, Sebastian Rafael, Rodriguez José Félix, Lekadir Karim, Frangi Alejandro F. An atlas- and data-driven approach to initializing reaction-diffusion systems in computer cardiac electrophysiology. *Int J Numer Method Biomed Eng.* 2017;.

[31] Orosio J., Rajandra A., Bubien R., Arciniegas J.. Continuous Multi-Electrode Mapping: Single-Center Experience. *EP Lab Digest.* 2016;16(1).

[32] Koutalas Emmanuel, Rolf Sascha, Dinov Borislav, et al. Contemporary Mapping Techniques of Complex Cardiac Arrhythmias - Identifying and Modifying the Arrhythmogenic Substrate. *Arrhythm Electrophysiol Rev.* 2015;4(1):19-27.

[33] Durrer D, Dam R T, Freud G E, Janse M J, Meijler F L, Arzbaecher R C. Total excitation of the isolated human heart. *Circulation.* 1970;41(6):899-912.

[34] Abboud S, Berenfeld O, Sadeh D. Simulation of high-resolution QRS complex using a ventricular model with a fractal conduction system. Effects of ischemia on high-frequency QRS potentials. *Circ Res.* 1991;68(6):1751-60.

[35] Atkinson Andrew, Inada Shin, Li Jue, et al. Anatomical and molecular mapping of the left and right ventricular His-Purkinje conduction networks. *J Mol Cell Cardiol.* 2011;51(5):689-701.

[36] Liu Benjamin R., Cherry Elizabeth M.. Image-Based Structural Modeling of the Cardiac Purkinje Network. *BioMed Research International.* 2015;2015(621034):1 -15.

[37] Rotter Martin, Takahashi Yoshihide, Sanders Prashanthan, et al. Reduction of fluoroscopy exposure and procedure duration during ablation of atrial fibrillation using a novel anatomical navigation system. *Eur Heart J.* 2005;26(14):1415-21.